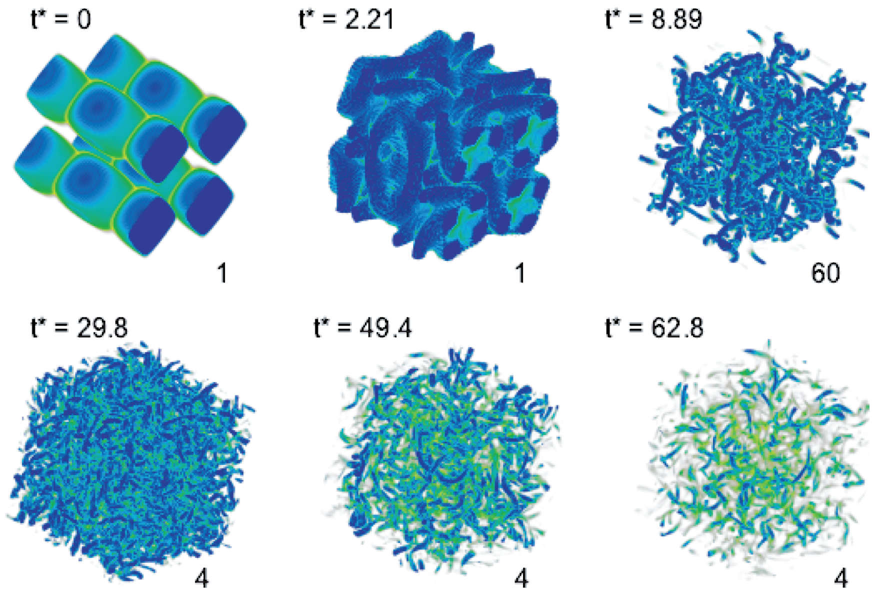

Plate 1. (Fig. 4a.6) Flow visualizations of the TGV flow, using volume renderings of λ_2. The results shown here (representative of all methods discussed) are from the fourth-order 3D monotone FCT on the 128^3 grid.

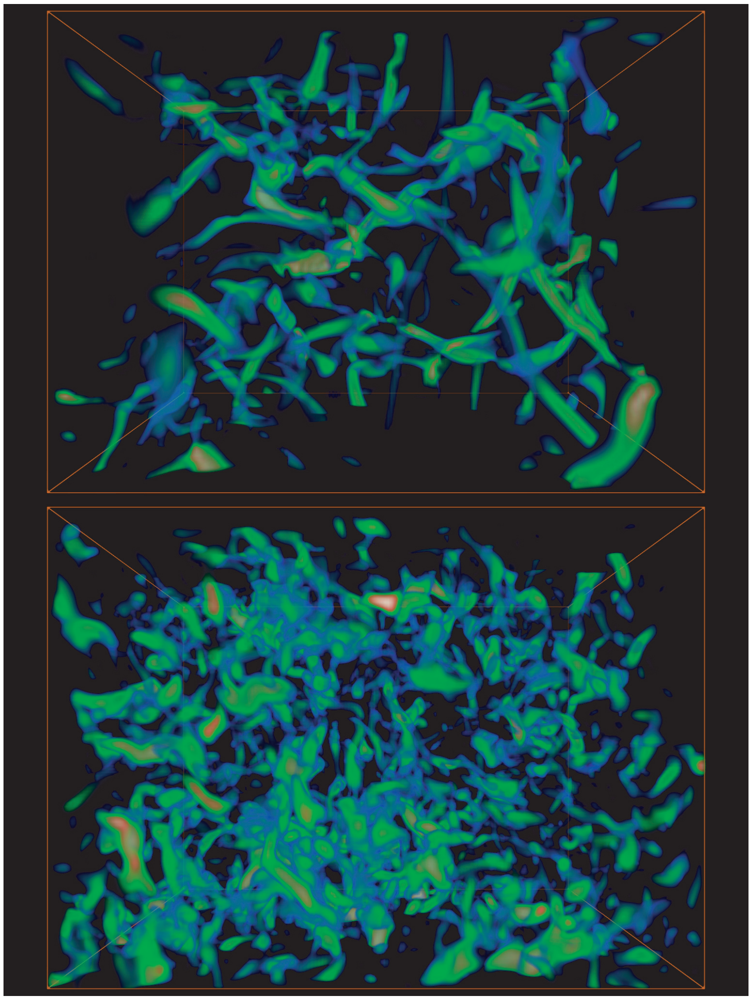

Plate 2. (Fig. 7.1) Two contrasting visualizations of homogeneous, compressible turbulence as computed on a 1024^3 grid with the PPM scheme in 1993. In the upper panel, vorticity structures near the dissipation range of length scales are shown in a small region of the fully developed turbulent flow. In the lower panel, the data have been filtered before the vorticity image was rendered. These vorticity structures are in the Kolmogorov inertial range of length scales. Each region shown is the same width relative to that of the vortex tubes it contains. The two images here were rendered for direct and unbiased comparison. In each subvolume shown, the same volume fraction is occupied by each opacity–color level. The very different appearance of these images therefore reflects real differences in their dynamics. The relatively straight vortex tubes near the dissipation range do not readily kink to form still smaller structures.

Plate 3. (Fig. 7.4) Volume rendering of a thin diagonal slice through the cube of turbulence computed at NCSA in 2003 with our PPM–Euler code on a grid of 2048^3 cells. The logarithm of the vorticity magnitude is shown. The flow is shown at 1.15 sound or flow-crossing times (the initial rms velocity is Mach 1) of the energy-containing scales, which are half the size of the cubical computational domain. At this stage it is clear that small-scale turbulence is developing more rapidly in some regions of this flow than in others, despite the statistical homogeneity imposed on the initial condition for the problem. Analysis of the flow on larger scales in these regions can reveal why the turbulence is developing rapidly there and not elsewhere.

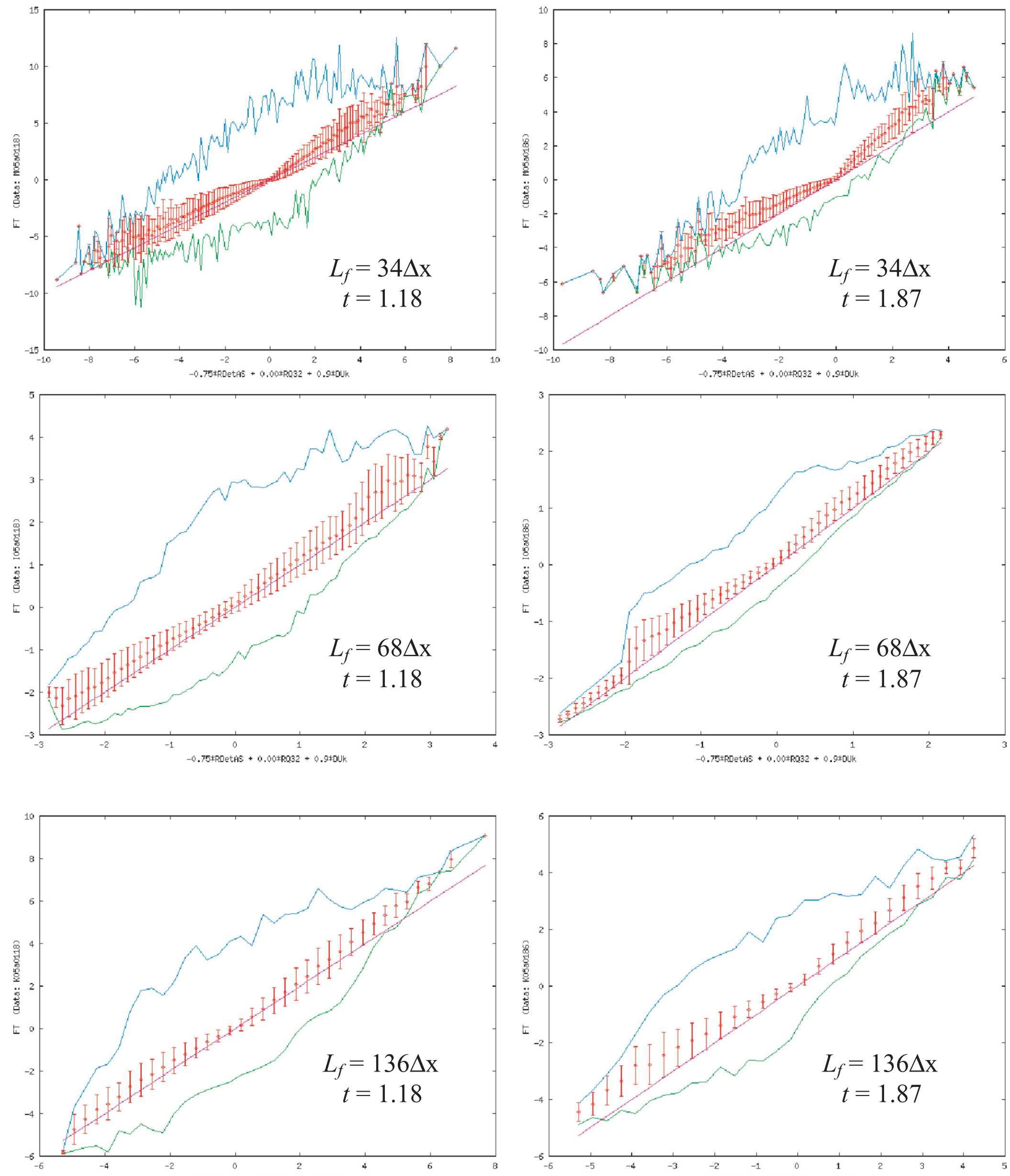

Plate 4. (Fig. 7.5) Data from a PPM simulation of homogeneous, Mach 1, decaying turbulence on a grid of 2048^3 cells (Woodward et al. 2004) was used to evaluate the term $F_{SGS} = -\tau_{ij}\ \partial_j\ \partial\tilde{u}_i$ at two different times and using three different Gaussian filter widths. F_{SGS} is plotted as the ordinate, and the corresponding values of the model equation discussed in the text are plotted as the abcissa. The two quantities are seen to be well correlated for this run.

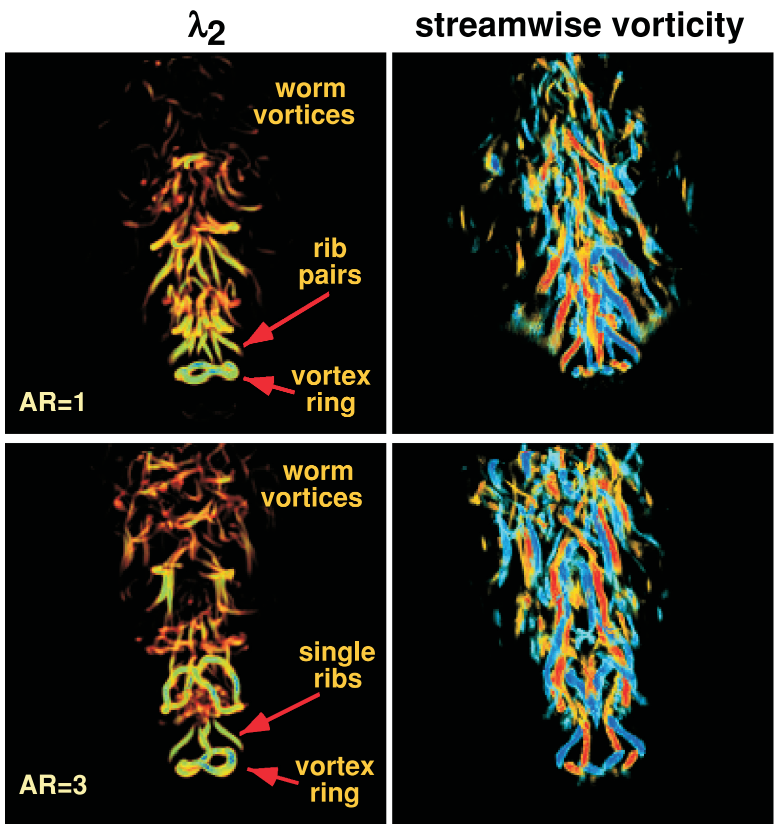

Plate 5. (Fig. 8.5) Comparative instantaneous visualizations based on volume visualizations of λ_2, the second-largest eigenvalue of tensor $\mathbf{S}^2 + \Omega^2$, where $\mathbf{S}$ and Ω are the symmetric and antisymmetric components of the velocity gradient tensor, are shown on the left. Corresponding visualizations of the streamwise vorticity are shown on the right.

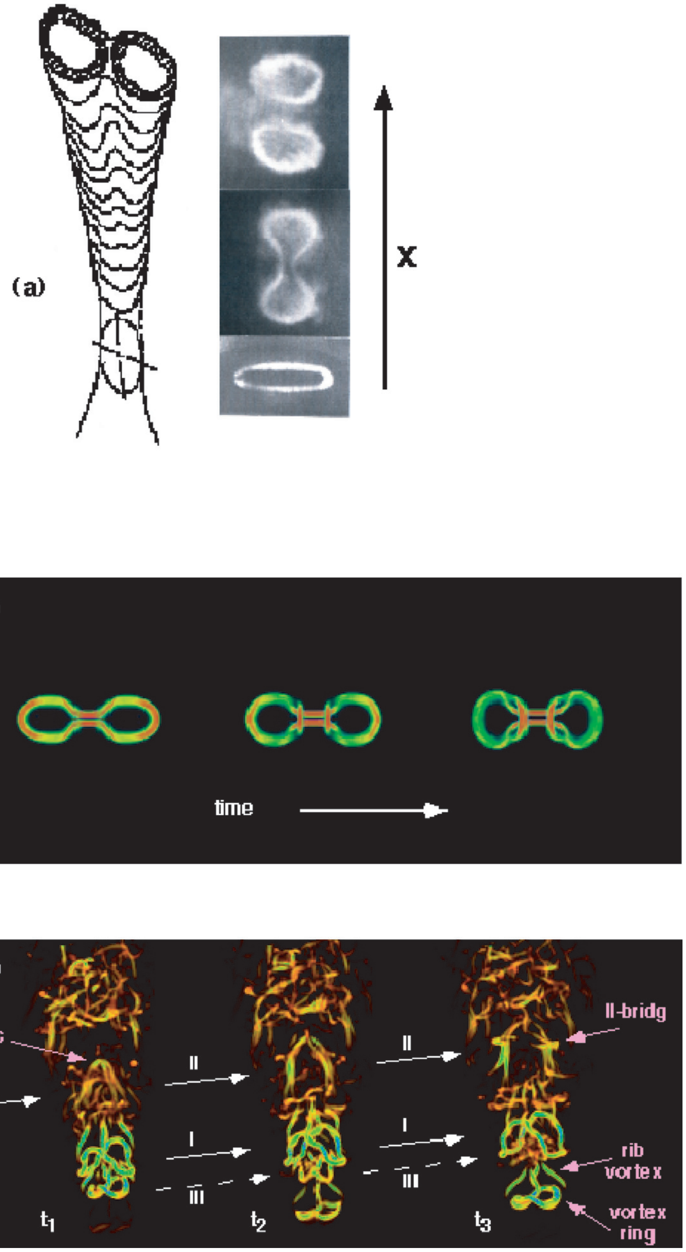

Plate 6. (Fig. 8.6) (a) Characteristic axis-switching and bifurcation phenomena for AR = 4 from visualizations of laboratory elliptical jets subject to strong excitation at the preferred mode (Hussain and Husain 1989); (b) visualizations of an AR = 4 rectangular jet based on ILES data (Grinstein 1995); (c) ILES simulation of an AR = 3 rectangular jet (Grinstein 2001).

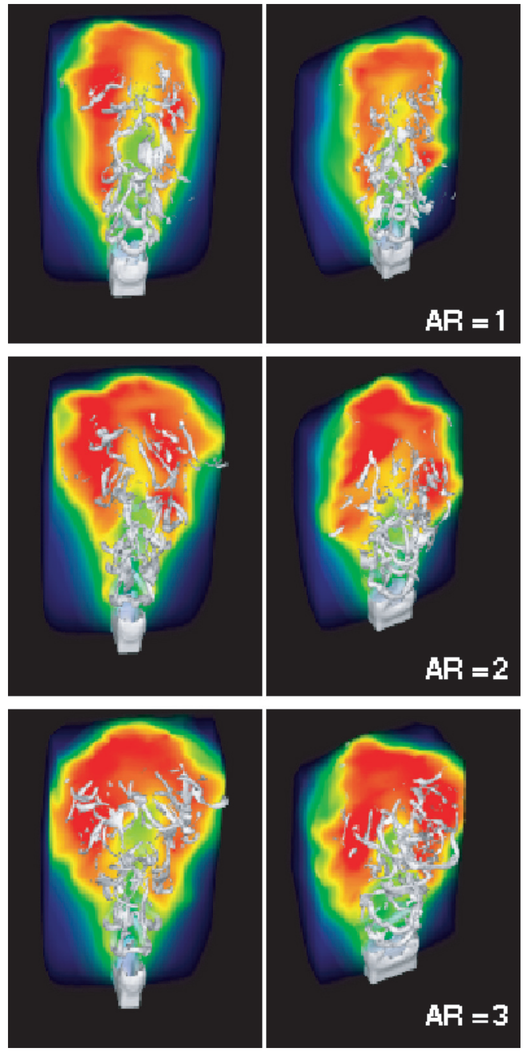

Plate 7. (Fig. 8.9) Instantaneous visualizations of non-premixed-combustion regions as a function of AR at two selected times (Grinstein 2001). Temperature distributions in the back half of the visualized subvolume are superimposed to isosurfaces of the vorticity magnitude (gray).

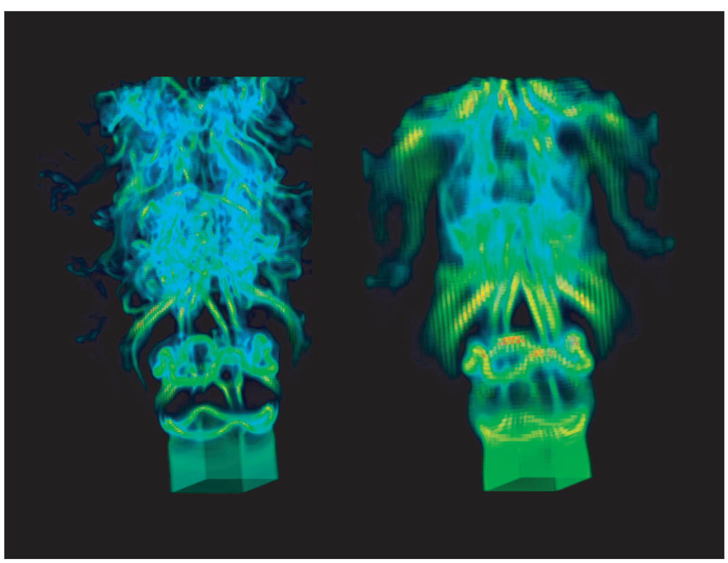

Plate 8. (Fig. 8.10) Comparative instantaneous volume visualization of the vorticity magnitude based on the database of square jets at the same time simulations on the finest grid, left, and coarsest grid, right (from Grinstein 2001).

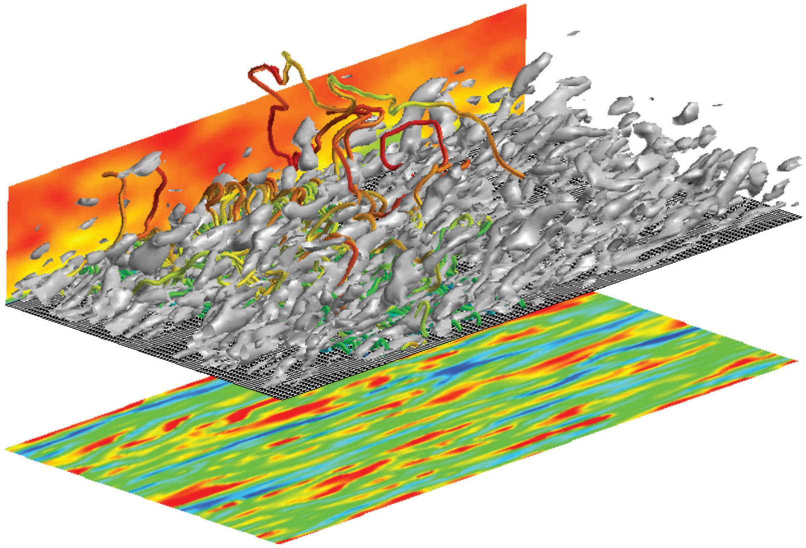

Plate 9. (Fig. 10.1) Fully developed turbulent channel flow: Perspective of a fully developed turbulent channel flow at $Re_\tau = 1800$ from ILES, together with the wall model (ILES + WM) using the FCT algorithm.

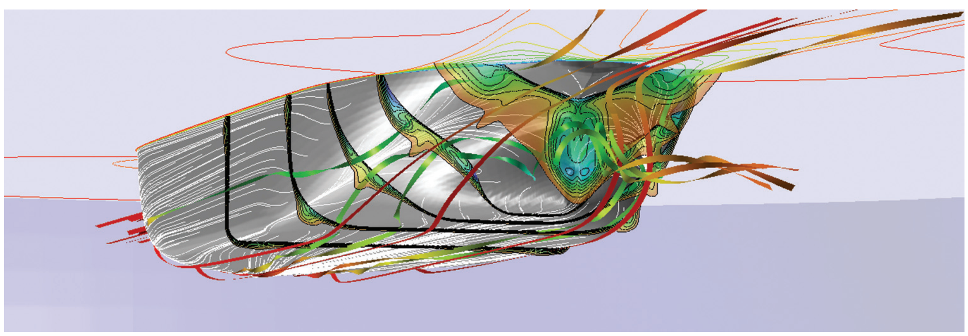

Plate 10. (Fig. 10.14) Ship flow: Perspective view from the stern of the flow past the KVLCC model, showing the time-averaged boundary layer profiles, surface streamlines, and streamlines released at the bow.

Plate 11. (Fig. 14.1) Geophysical turbulence. Scales of motion $\mathcal{O}(10^7)$, $\mathcal{O}(10^4)$, and $\mathcal{O}(10^{-2})$ m, from left to right, respectively.

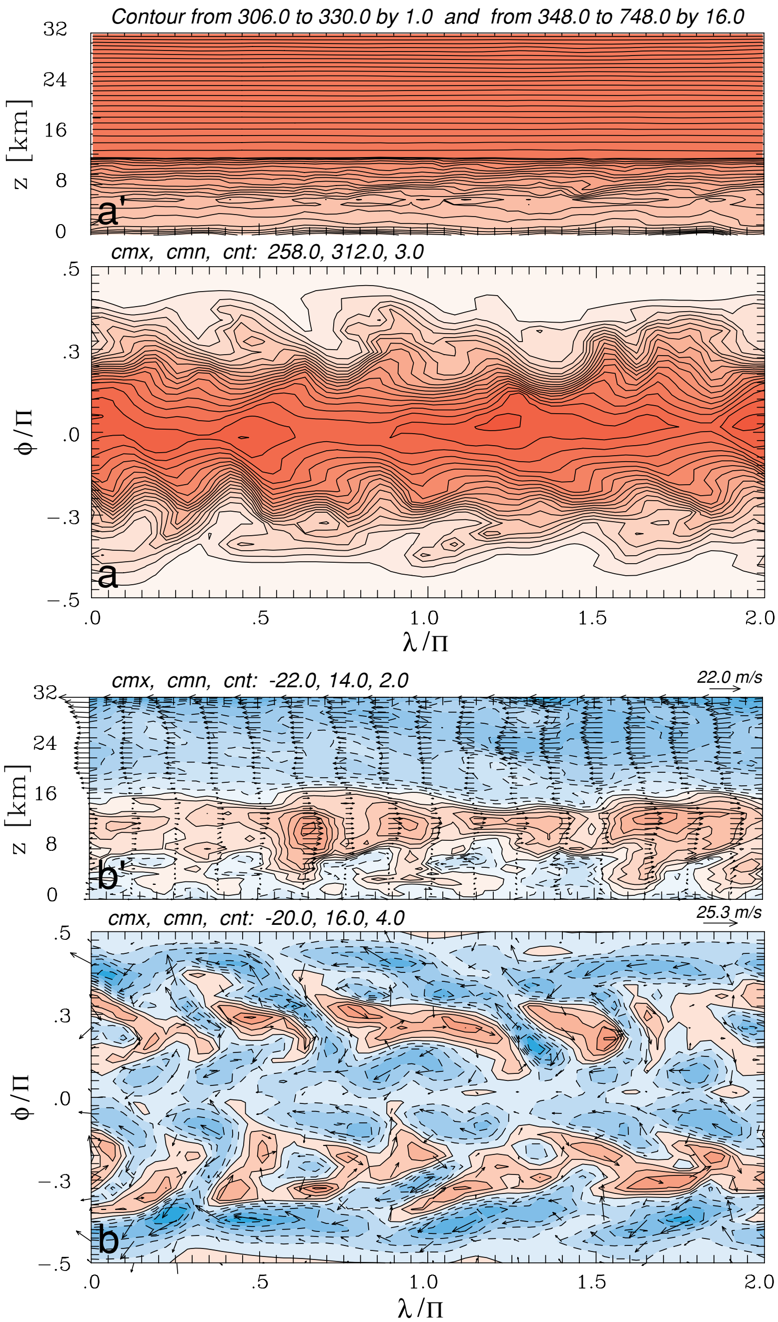

Plate 12. (Fig. 14.7) Instantaneous solutions of the idealized climate problem after 3 years of simulation.

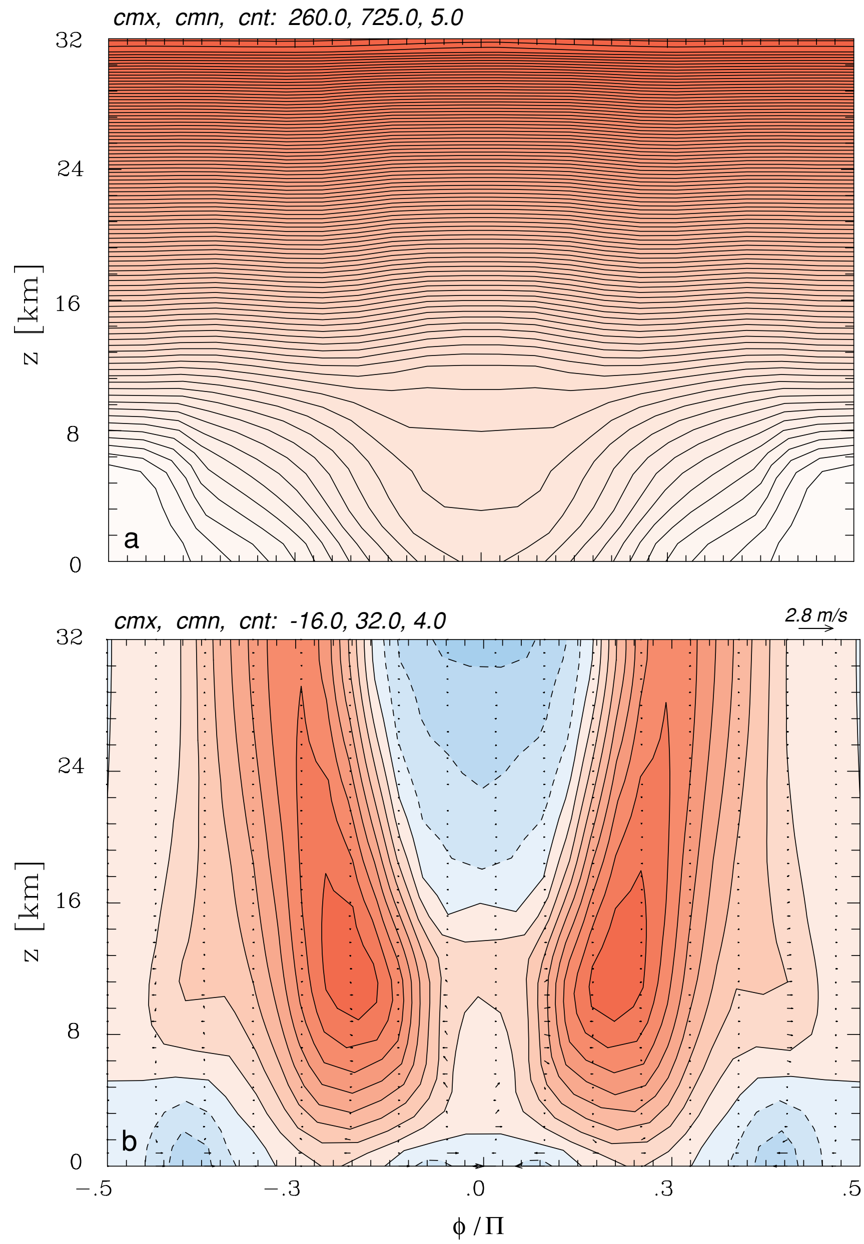

Plate 13. (Fig. 14.8) The zonally averaged 3-year means of potential temperature (plate a) and zonal velocity (plate b) for the simulation highlighted in Figure 14.7. The contouring convention is similar to that used in Figure 14.7.

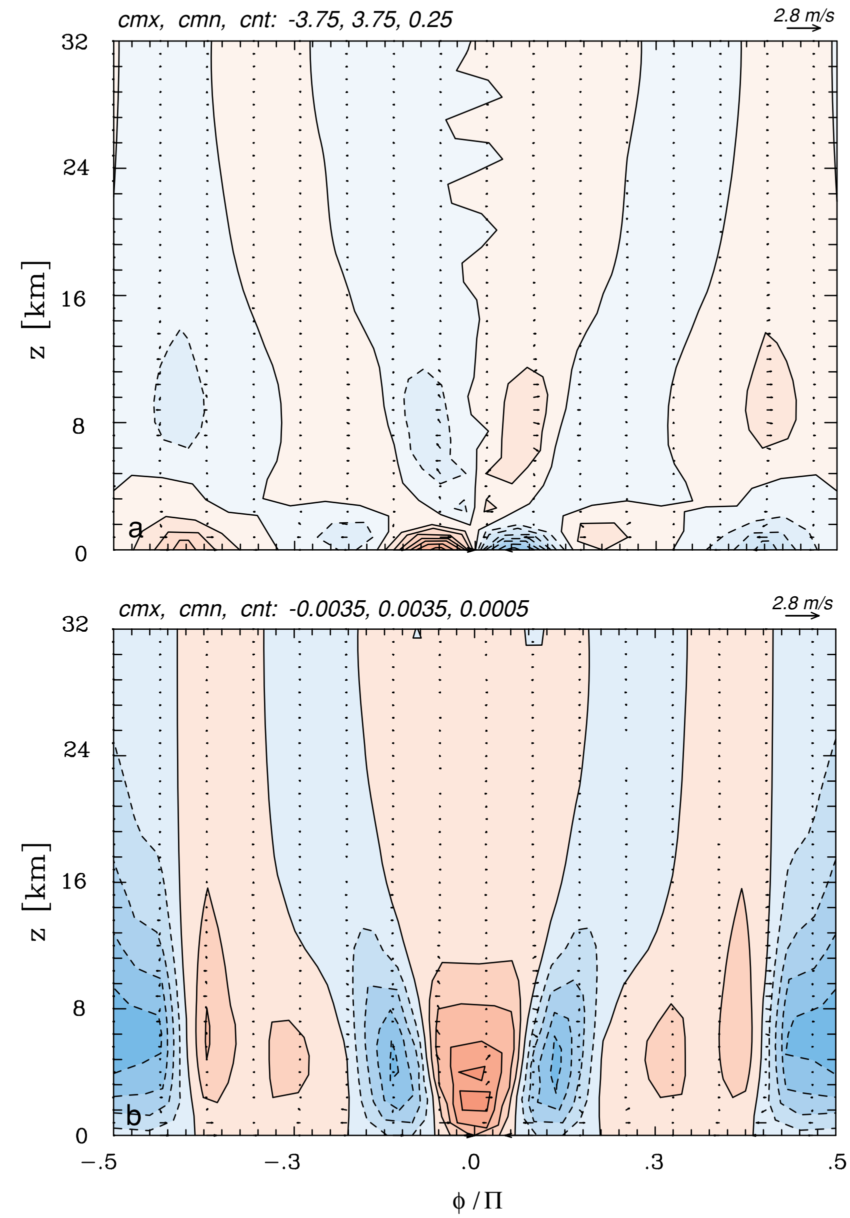

Plate 14. (Fig. 14.9) The zonally averaged 3-year means of meridional and vertical velocities (plates a and b, respectively) for the simulation highlighted in Figure 14.7.

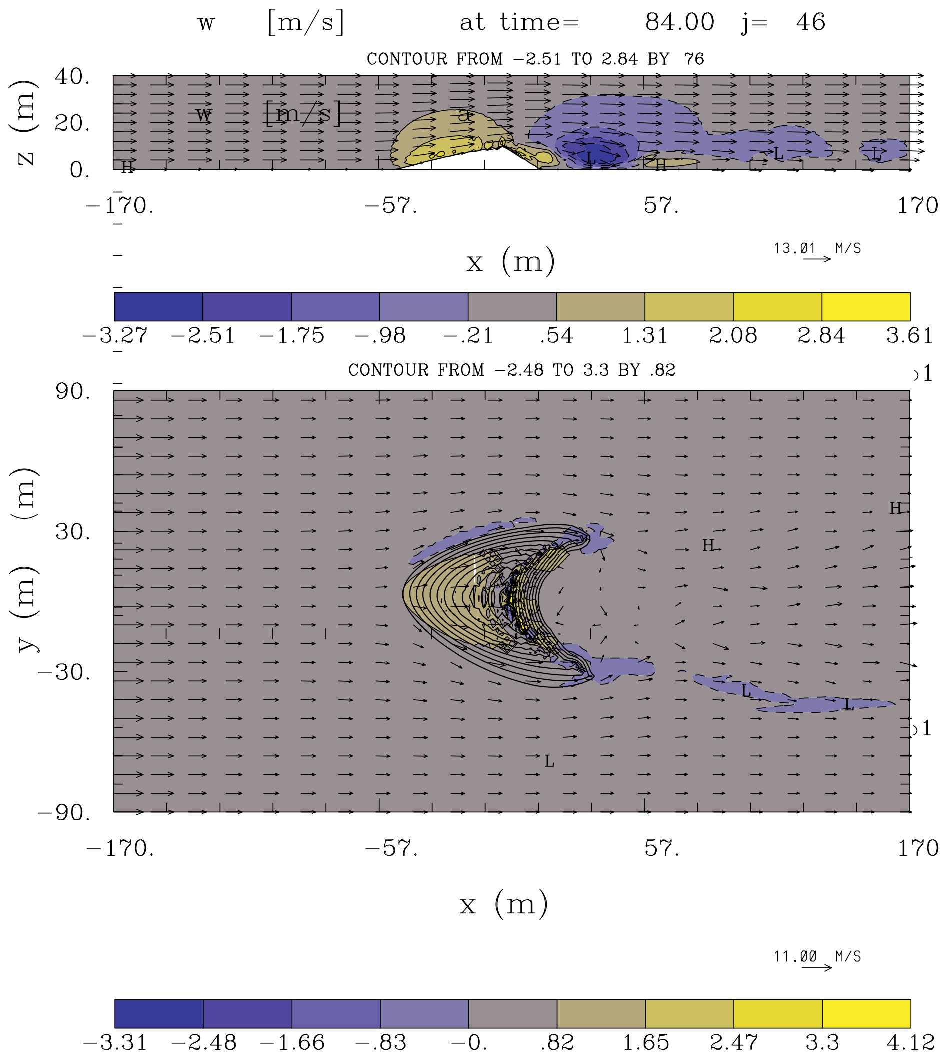

Plate 15. (Fig. 14.10) LES of a PBL past a rapidly evolving sand dune.

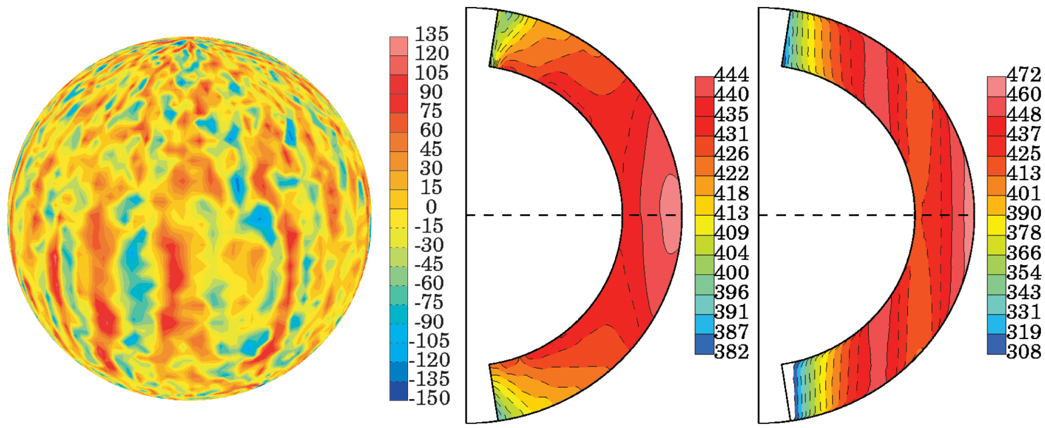

Plate 16. (Fig. 14.12) NFV simulations of solar convection. The left panel shows the vertical velocity (ms^{-1}) on a horizontal surface near the middle of the domain for the ILES run. Central and right panels show the time-averaged angular velocity (nHz) for, respectively, DNS and ILES runs.

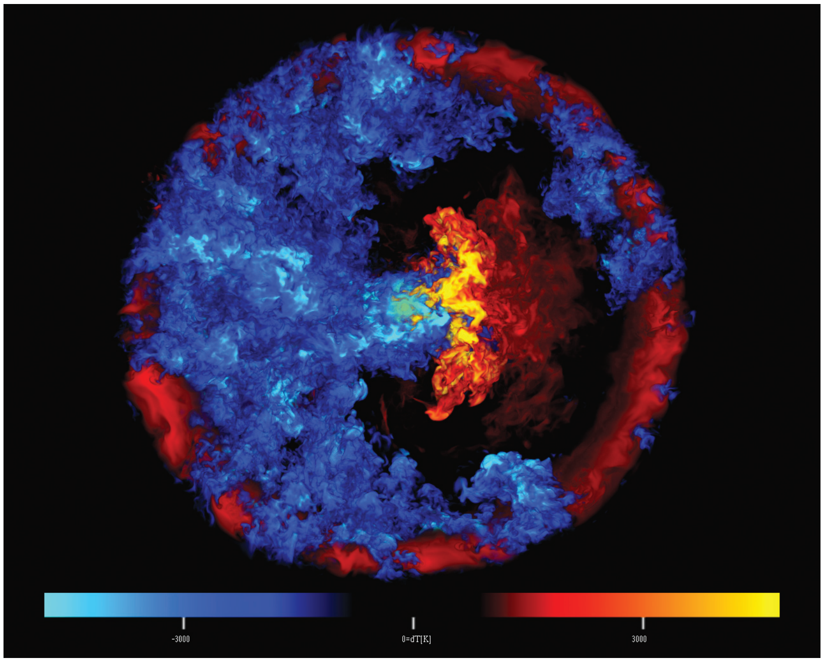

Plate 17. (Fig. 15.14) Temperature fluctuations in a thick section from a simulation of convection in spherical geometry. this section passes through the center of the model and is aligened to cut through the principle down flow plume, which is seen as cool gas (blue and aqua hues) on the left side of the figure.

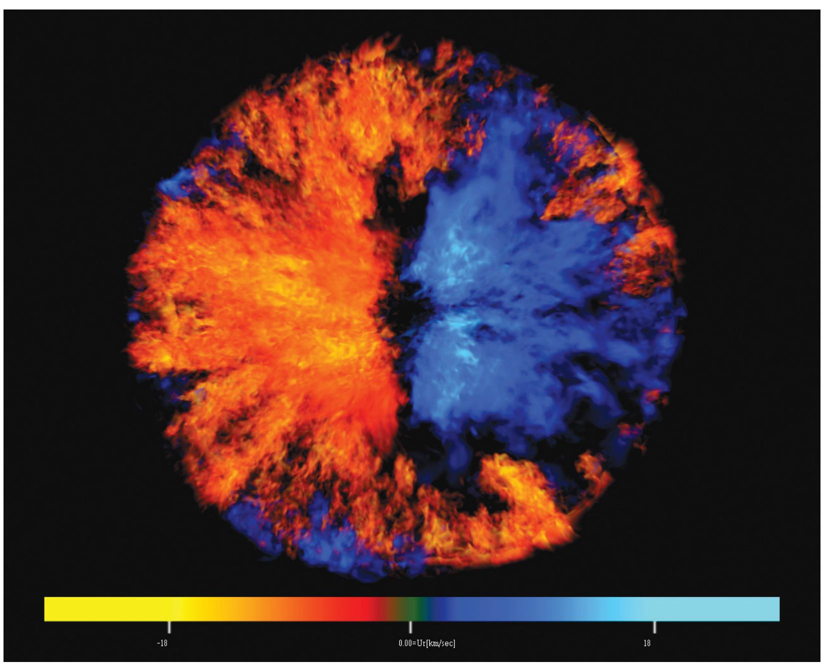

Plate 18. (Fig. 15.16) Radial velocity in a thick section. The predominantly negative (crimson hues) and positive (blue and aqua) radial velocities on the left and right sides of this figure correspond to a dipolar flow.

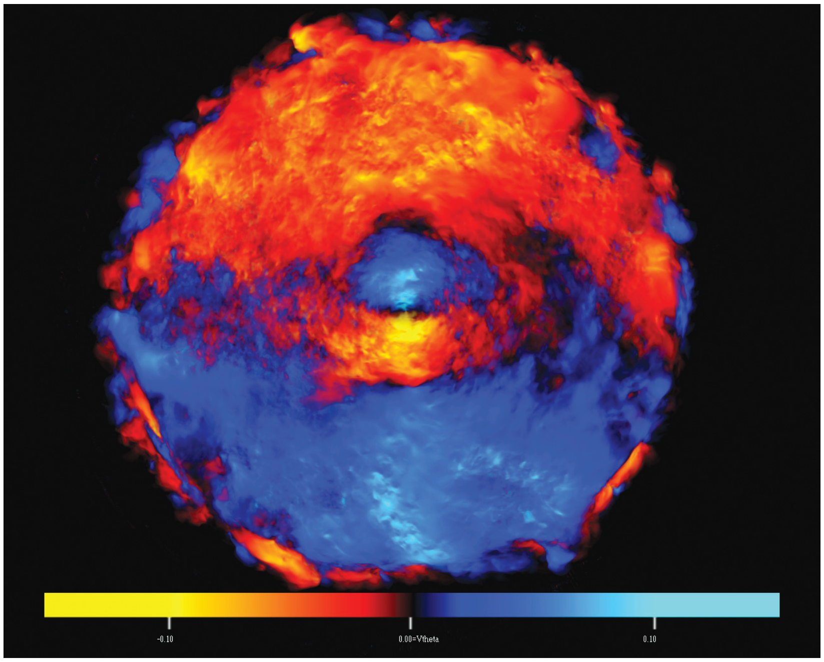

Plate 19. (Fig. 15.17) Angular component of velocity from a simulation of convection in spherical geomety. The view, orientation, and section shown here are the same as those used in figures 15.14 and 15.16. Negative (crimson hues) and positive (aqua hues) values of angular velocity correspond to counterclockwise and clock wise motion about the axis along the line of sight through the center of the model. The predominant pattern of angular motion indicates a dipolar flow filling the interior of the star.

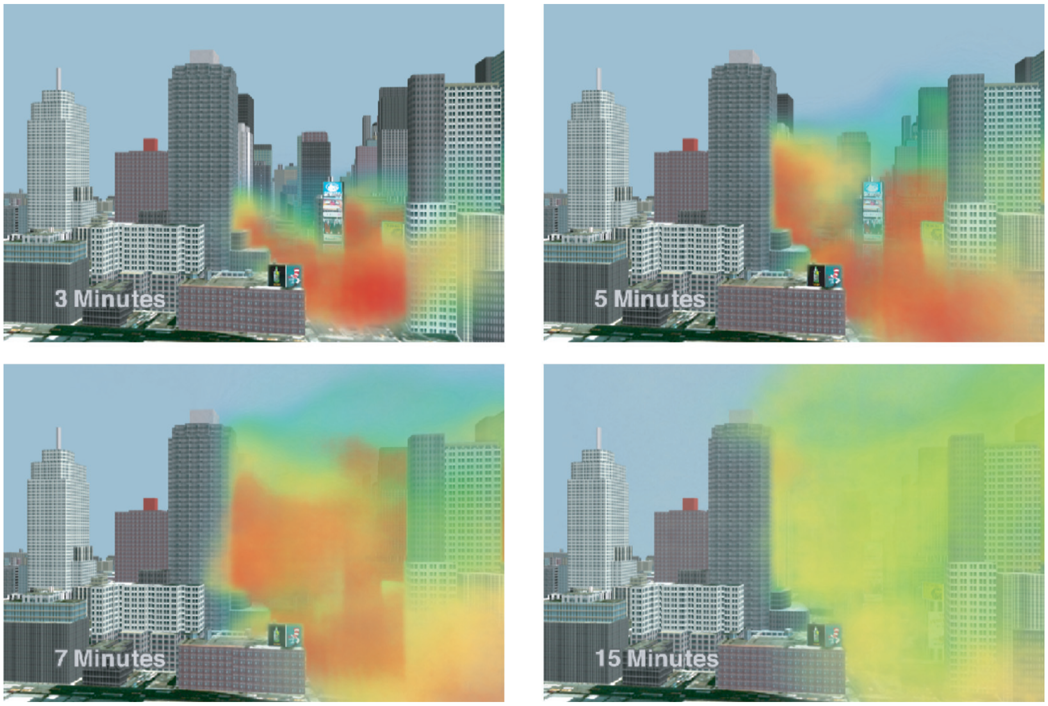

Plate 20. (Fig. 17.3) Contaminant dispersion from an instantaneous release in Times Square, New York City, as predicted by the FAST3D-CT MILES model. The frames show concentrations at 3, 5, 7, and 15 min after release.